Nucleic Acids Research, 2025, **53**, gkaf227
https://doi.org/10.1093/nar/gkaf227
Nucleic Acid Enzymes

Self-contained G-quadruplex/hemin DNAzyme: a superior ready-made catalyst for *in situ* imaging analysis

Jia Li[1,†], Lanxin Jiang[1,†], Haiping Wu[2,†], Yuting Zou[1], Shasha Zhu[1], Ying Huang[1], Xinping Hu[1], Huili Bai[1], Ying Li[1], Yuan Zou[3], Shijia Ding[3], Wei Cheng[1,*]

[1]Department of Clinical Molecular Medical detection center, Laboratory medicine center, The First Affiliated Hospital of Chongqing Medical University, Chongqing 400016, P.R. China
[2]Sichuan Provincial Key Laboratory for Human Disease Gene Study and the Center for Medical Genetics, Department of Laboratory Medicine, Sichuan Academy of Medical Sciences and Sichuan Provincial People's Hospital, University of Electronic Science and Technology of China, Chengdu 611731, P.R. China
[3]Key Laboratory of Clinical Laboratory Diagnostics (Ministry of Education), College of Laboratory Medicine, Chongqing Medical University, Chongqing 400016, P.R. China

To whom correspondence should be addressed. Email: chengwei@hospital.cqmu.edu.cn
[†]The first three authors should be regarded as Joint First Authors.

Abstract

The G4 DNAzyme holds significant potential for applications in bioanalysis and determination owing to its peroxidase mimetic activity and DNA programmability. However, its clinical practicability is constrained by limited catalytic activity and supplementary assembly requirements, attributed to weak π–π stacking, deficient active-site components, and ion-dependent assembly mechanisms. Thus, we constructed a highly active self-contained intramolecular G4/hemin DNAzyme through the direct covalent cross-linking of catalytic core components involving the hemin prosthetic group, G4 pocket, and distal ligand-like assistant nucleotide (adenine or cytosine). Detailed investigations of the catalytic efficiency and mechanism confirmed the formation of a compact catalytic active center through covalent bonding, which enhanced the catalysis to a stage comparable to that of horseradish peroxidase in localized surroundings. The superior ready-made catalytic modularity with programmability enabled the highly sensitive *in situ* imaging analysis of HER2 protein in breast cancer specimens. This study provides a powerful tool for disease marker imaging detection with high sensitivity and immediate availability.

Graphical abstract

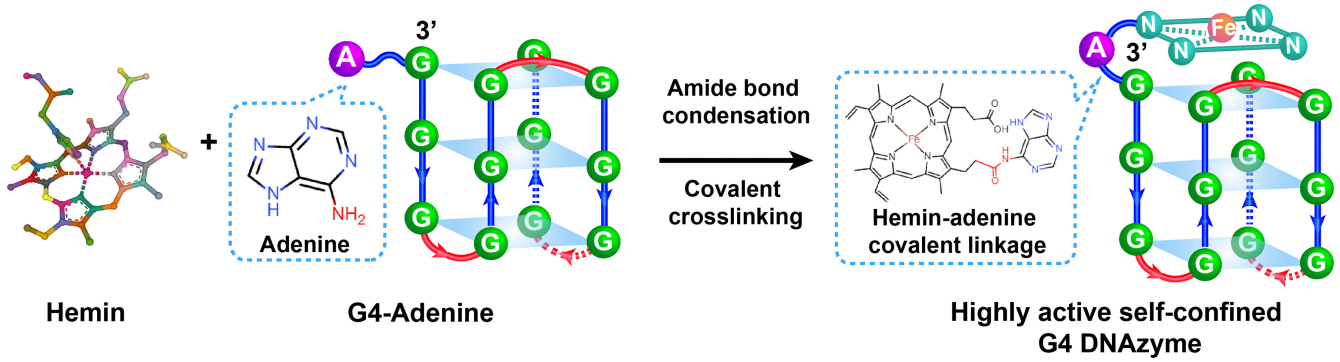

Introduction

Artificial enzymes can be engineered and programmed via biomimetic design to achieve or surpass the catalytic efficiency of natural enzymes [1, 2]. They have been extensively applied in biomedicine and environmental protection [3–5]. The G-quadruplex (G4) peroxidase-mimicking DNAzyme exhibits the manipulability and programmability of nucleic acids and has been continuously modified for optimal performance [6–8]. The G4 with flexible sequences and structures binds to hemin, a crucial cofactor in catalytic activity, through stacked G-tetrads induced by hydrogen bonding to form the G-quadruplex/hemin DNAzyme (G4/hemin) with horseradish peroxidase (HRP)-mimicking activity [9, 10]. The G4/hemin complex offers the advantages of its small size, facile synthesis and manipulation, susceptibility to rational design through allosteric control, and broad applications in

Received: December 13, 2024. **Revised:** March 5, 2025. **Editorial Decision:** March 6, 2025. **Accepted:** March 11, 2025

bioanalytical and biomedical fields [4, 11–13]. However, its limited catalytic capacity and supplementary assembly requirements hinder its clinical practicability.

Many strategies have been proposed to improve the performance of G4/hemin. Such strategies have been focused on its catalytic core structure, which includes a hydrophobic hemin-binding site provided by the G4 pocket, guanine bases functioning as the proximal axial ligand of hemin, and a distal ligand responsible for general acid–base catalysis [14–16]. For the G4 pocket, structural transformation due to sequence differences, particularly in flanking regions, suggests that the parallel structure exhibits better performance than mixed and hybrid forms, which is related to ion induction [17–20]. The modulation of distal ligand analogs, either by exogenous addition [adenosine triphosphate (ATP) or spermidine] or internal nucleobase modification [adenine (dA) or cytosine (dC)] is widely acknowledged as highly effective for promoting catalysis [21–24]. This process mimics an adjustable histidine reagent that performs general acid–base catalysis and activates H_2O_2 prototropic cleavage during peroxidase catalysis, thereby improving catalytic performance [25]. In addition to the investigation of individual G4 sequences and nucleobase modifications, covalent modification with hemin represents another significant approach for G4 DNAzyme enhancement. Several studies have investigated the simple covalent conjugation of G4 sequences with hemin, exploring their catalytic capabilities, mechanisms, and applications [e.g. immunohistochemistry (IHC) and chemiluminescence] [26–28]. Importantly, hemin-related covalent modifications, including free non-G4 sequences, G4, amino acids, and short peptides, are gradually overcoming the weak catalytic capacity limitation of DNAzymes and addressing the limitations of traditional proteases, leading to the evolution of DNAzymes [11, 29–31].

Our previous studies have demonstrated that the covalent attachment of hemin plays a unique role in enhancing its activity owing to its increased solubility [32, 33]. Furthermore, the zippered G4/hemin DNAzyme (Z-G4/H), formed through short-oligonucleotide covalent-hemin neighbor hybridization with G4 sequences, exhibits excellent catalytic capabilities, a more rapid catalytic rate, and high environmental tolerance compared with that of classic G4/hemin DNAzymes (C-G4/H) [34]. The close physical proximity of hemin (catalytic active center) to the dA/dC (distal ligand analog supplement)-modified G4 structure through adjacent hybridization contributes to the high performance of DNAzymes [14, 25]. However, the conventional ion-dependent assembly and zippered hybridization assembly of G4 DNAzymes involve the intermolecular assembly of catalytic core components through the weak π–π stacking of noncovalent bonds [35]. This intermolecular assembly impacts the extent of tight binding at the catalytic active center of the DNAzyme, constraining its catalytic capacity [14]. Furthermore, owing to the ion-dependent assembly and hybridization process of DNAzymes, they are not readily available for immediate use, which limits their practicability [19].

Thus, according to the distance-dependent organization of catalytic active centers reported in prior research, we engineered a covalently nucleotide-modified G4-hemin DNAzyme complex (Co-G4N/H) through the direct covalent cross-linking of the hemin prosthetic group, ligand-like assistant nucleotide, and G4 structure to achieve enhanced catalytic performance. The intramolecular Co-G4N/H functions as a self-contained DNAzyme, featuring a tightly bound active center connected by a robust covalent bond, offering an enhanced and ready-made catalyst for high efficiency and immediate application. We investigated its performance and advantages in bulk and localized surroundings, as well as catalytic characteristics and efficient assembly principles. Notably, several studies investigating the simple covalent conjugation of G4 with hemin and the enhancement of the G4 DNAzyme catalytic performance using adjacent adenine nucleotides have been conducted. Considerably, we construct a G4 DNAzyme that mimics HRP through the tight conjugation of three catalytic core component. Ultimately, the Co-G4N/H formed by the covalent conjugation of the three components exhibits significantly higher catalytic efficiency and stability than the simple-covalent G4 DNAzyme and noncovalent adenine-modified G4 DNAzyme. Furthermore, we employed the cell surface HER2 protein, which is considered a superior marker for the diagnosis and targeted drug therapy of breast cancer, as a paradigm [36, 37]. Leveraging the programmability and immediate availability of Co-G4N/H, we propose a highly sensitive and practical approach for detecting the HER2 protein on the surface of breast cancer cells. Thus, a robust grading application of HER2 protein was achieved in formalin-fixed paraffin-embedded (FFPE) tissue specimens from patients with breast cancer.

Materials and methods

Materials and reagents

All the DNA oligonucleotide sequences used in this study and the related abbreviations are listed in Supplementary Table S1. Unmodified DNA oligonucleotides were synthesized by Sangon Biotech (Shanghai) Co. Ltd. Modified and high-performance liquid chromatography-purified oligonucleotides were obtained from Takara Biotechnology (Dalian, China). Their concentrations were determined by measuring the absorption values at 260 nm obtained via ultraviolet–visible (UV–VIS) spectroscopy and the extinction coefficients provided by Integrated DNA Technologies (OligoAnalyzer v3.1 tool, http://sg.idtdna.com/calc/analyzer). All the oligonucleotides were dissolved in a 1 × Tris-EDTA (TE) buffer (10 mM Tris–HCl, 1 mM ethylenediaminetetraacetic acid, pH = 8.0) and stored at −20°C. All the other reagents were of analytical grade. All the buffer solutions were prepared using Millipore-Q water (≥18 M, Milli-Q, Millipore). G4s were prepared by heating the DNA samples at 95°C for 5 min, followed by overnight cooling to room temperature (RT) and storage at 4°C until use.

Hemin; 2,2′-azino-bis (3-ethylbenzothiazoline-6-sulfonic acid ($ABTS^{2-}$); luminol; polyethylene glycol 4000 (PEG4000); absolute ethanol; HRP; and dimethyl sulfoxide (DMSO) were purchased from Sangon Biotech (Shanghai) Co. Ltd. The fluorescent substrate 10-Acetyl-3,7-dihydroxyphenoxazine (ADHP) was purchased from TargetMol (Shanghai, China). Hemin and ADHP were dissolved in DMSO as a stock solution and diluted to the required concentration using a 50 mM Tris–HCl buffer (pH = 7.0, 25 mM KCl) prior to use. Freshly prepared $ABTS^{2-}$ and luminol were dissolved in ultrapure water to a concentration of 4 mM prior to use. HRP and PEG4000 were dissolved in ultrapure water to concentrations of 200 and 25 mg/ml prior to use, respectively. Except for the pH and ion analyses, all the experiments were per-

formed in 50 mM Tris–HCl (pH = 7, 25 mM KCl). Tetraethyl orthosilicate (98%) was purchased from Sigma–Aldrich. SU8-3035 and propylene glycol methyl ether acetate were purchased from Suzhou Research Materials Micro-Tech. Fluorocarbon oils, HFE-7100 and HFE-7500, were purchased from 3M. The silicone elastomer polydimethylsiloxane (PDMS) was purchased from the Dow Chemical Company.

Measurement of DNAzyme activity

The annealed classic G4 sequences (C-G4s) (45 nM) diluted from the corresponding stock solution were incubated with hemin (45 nM) in a 50 mM Tris–HCl buffer for 30 min at 37°C to form G4/hemin complexes. Covalent G4 probe was directly diluted to a concentration of 45 nM. The HRP concentration was 2 μg/ml. Thereafter, $ABTS^{2-}$ (2 mM) and H_2O_2 (50 mM) were added. Afterward, the products were analyzed via UV–VIS spectroscopy over the range of 400–500 nm. Experiments on catalytic kinetics were performed at 418 nm for 150 s. The initial rate (V0, nM/s) of the oxidation reaction was calculated from the slope of the linear portion of increases in the concentration of $ABTS^{\bullet-}$ versus time (25 s). The $ABTS^{\bullet-}$ concentration was calculated based on the extinction coefficient of $ABTS^{\bullet-}$ (36 000 $M^{-1}\cdot cm^{-1}$). For fluorescence experiments, HRP (0.4 μg/ml) and G4 DNAzymes (9 nM), ADHP (100 nM), and H_2O_2 (1 mM) were mixed, and the products were analyzed via fluorescence spectroscopy over the range of 550–650 nm. Experiments on catalytic kinetics were performed at 585 nm for 200 s. For chemiluminescence experiments, HRP (2 μg/ml) and G4 DNAzymes (45 nM), luminol (2 mM), and H_2O_2 (50 mM) were mixed, and the products were analyzed using a microplate reader for 120 s.

Circular dichroism measurements

Circular dichroism (CD) spectra were recorded using a CD spectropolarimeter (Applied Photophysics) over a wavelength range of 200–350 nm. The G4 solutions (5 μM) were obtained by directly diluting DNA stock solutions with 50 mM Tris–HCl buffers (pH = 7.0, with or without 25 mM KCl). A lamp was placed under a stable stream of dry purified nitrogen (99.99%) during experimentation.

Analysis of interactions between G4 and hemin molecules

The 3D-NuS program (specializing in G4 construction) was employed to predict and model the finalized 3D structure of G4. The hemin molecule was docked via noncovalent docking, and the covalent-hemin molecule was docked via covalent docking. Molecular docking was implemented using the AutoDock 4.2.6 software package in a global docking manner. The docking time was set to 50, and the rest of the parameters were taken as default values.

Decay kinetics of DNAzymes and DNAzyme activities under different conditions

H_2O_2 (2 mM) was added to evaluate the decay kinetics of the G4 DNAzymes (1 μM) by recording the absorbance at 402 nm over time. The activities of the DNAzymes at different pH levels were evaluated in a 20 mM Britton–Robinson buffer (pH = 2.83–7.08, 20 mM acetic acid, 20 mM orthophosphoric acid, 20 mM boric acid, and 100 mM KCl). The activities of the DNAzymes at different H_2O_2 concentrations were investigated in a Tris–HCl buffer containing 5, 10, 25, 50, 100, and 250 mM H_2O_2, respectively. The activities of the DNAzymes under different K^+ conditions were investigated in a Tris–HCl buffer containing 0, 5, 10, 25, 50, 75, and 100 mM K^+, respectively. The data were converted into V0 values, as described above. All the measurements were performed in triplicate.

Fabrication of droplet generation microchip

A microfluidic chip was fabricated via soft lithography technology. The AutoCAD software was employed to design the pattern, which was transferred to the photomask. Thereafter, the SU-8 3035 photoresist was coated onto the silicon wafer and solidified via ultraviolet exposure to specific areas protected by the photomask. After developing the photoresist and post-baking, the mold was produced. The silicone elastomer PDMS precursor (10:1) was poured onto the mold and cured at 75°C for 1 h to replicate the mold. Afterward, the patterned PDMS was peeled, punched with inlets and outlets, and bonded with a clean glass slide to form a complete microfluidic chip. Finally, 1% (w/w) perfluorodecyltriethoxysilane solution was injected into the channels, followed by incubation at 75°C for 1 h.

DNAzyme activities in localized droplets

Monodisperse microdroplets were generated from the flow-focusing nozzles of the microfluidic chips. HFE-7500 was selected as the continuous phase. The continuous and dispersed phases flowed at 0.3 and 0.1 ml/h, respectively. One side of the dispersed phase was injected with DNAzymes, and the other was injected with ADHP, H_2O_2, and PEG4000. After the droplets had stabilized, they were observed in the microfluidic chip groove or collected and dropped onto a microscope slide for observation.

Primer exchange reaction incubation and polyacrylamide gel electrophoresis characterization

A primer exchange reaction (PER) concatemer was synthesized using a reported method with minor modifications [38]. To enhance the signal intensity and sensitivity, we also designed and synthesized PER branch 1 (B1) and 2 (B2) and the corresponding signal output probes. The solution with a final concentration of 1 × phosphate-buffered saline (PBS) (100 μl), $MgSO_4$ (10 mM), dNTP (a mixture of equal molar ratios of dATP, dCTP, and dTTP; 300 μM), Bst LF polymerase (LF = Large Fragment; Bst = *Bacillus stearothermophilus*; 0.5 units/μl), Clean G (100 nM), and the hairpin (500 nM) was obtained. The sample was first incubated with Clean G at 37°C for 15 min to remove any potential dGTP to promote PER probe extension. The introduction of Clean G can eliminate any stuck primer and promote PER probe extension; a HER2 Apt-primer (10 μl, 1 μM) was added and incubated for another 1–4 h at 37°C. The reaction was ended by heating at 80°C for 20 min to inactivate the Bst LF polymerase. The length of the PER concatemers was characterized using 12% polyacrylamide gel electrophoresis (PAGE) at 110 V for 50 min at RT. The gel was imaged using a Bio-Rad ChemDoc XRS (Bio-Rad, USA) after GelRed staining for 30 min.

Characterization of PER concatemer with signal output probe in 96-well plates

A streptavidin-coated 96-well plate was blocked using 1% bovine serum albumin (BSA) and 0.4 mg/ml salmon sperm DNA for 1 h at RT [39]. Thereafter, different concentrations of the HER2 messenger RNA (mRNA)-biotin probe were added into a 200 μl PBS buffer for 1 h at 37°C. Afterward, the PER concatemer (100 nM) was incubated with the HER2 mRNA-biotin probe for another 2 h at 37°C. Next, the Fluor-488 P1 (300 nM), Co-G4A/H P1 (300 nM), and C-G4A/H P1 (300 nM) signal output probes were successively hybridized with the PER concatemer for 1 h at 37°C. After each step, the cells were washed in 0.1% Tween 20 in PBS thrice. Finally, the fluorescence spectra of the Fluor-488 probe were recorded from 530 to 590 nm at the excitation wavelength of 585 nm at 600 V. The fluorescence signal of the Co-G4A/H or C-G4A/H catalytic probe was recorded as previously mentioned.

In situ imaging of HER2 protein detection in breast cancer cells

To detect HER2 protein, human breast cancer cell lines SKBR-3, MDA-MB-231, and MCF-7 were seeded on glass coverslips pretreated with tissue culture in a 24-well plate and cultured in Dulbecco's modified Eagle's medium supplemented with 10% fetal bovine serum and 1% penicillin and streptomycin at 37°C in a 5% CO_2 incubator. When the cells had reached 60% confluence, they were fixed in 4% paraformaldehyde for 15 min at RT after the culture medium had been removed and washed thrice with ice-cold PBS. Endogenous peroxidase activity was inhibited using 3% H_2O_2 for 30 min. Nonspecific binding sites were blocked with a blocking buffer containing 3% BSA and 0.4 mg/ml salmon sperm DNA in PBS at 37°C for 1 h. The slides were washed twice using ice-cold PBS until analysis. To image the protein identity on the cell surfaces, the HER2-apt-PER concatemer (200 μl, 200 nM) was first added into 24-well plates for 1 h at 37°C. Thereafter, the 200 μl 1 μM Fluor-488, C-G4A/H, and Co-G4A/H signal probe systems were incubated with a cell for sufficient hybridization. After reacting with the corresponding probe at 37°C for 1 h, the slides were incubated with a tyramide reaction solution containing the Alexa Fluor™ 488 tyramide reagent (Tyr-488) (1:200) and 0.03% H_2O_2 at RT for 10 min in the dark in the Co-G4A/H or C-G4A/H catalytic probe system (the Fluor-488 system did not require this step). The cell nuclei were stained with a 4',6-Diamidino-2-Phenylindole (DAPI) solution. After each step, the cells were washed thrice in 0.05% Tween 20 in PBS for 5 min. The cells on the slides were analyzed using a Leica fluorescence microscope (Leica DM4000, Germany) with identical parameters for exposure. The fluorescence images of the cell slides were merged using the ImageJ v7.0. The HRP catalytic system for HER2 protein was assayed following the commercial tyramide signal amplification kit instructions (Invitrogen, USA).

For flow cytometry, a suspension of 10^6 cells was incubated with the corresponding probe system and reacted with a tyramide reaction solution. The fluorescence intensity of the cells was recorded using a Navios Series Flow Cytometer (Beckman Coulter International Trading Co., Ltd., China). The reagent used in this method was the Alexa Fluor 488-tyramine catalytic substrate, which exhibited the same excitation (495 nm) and emission (519 nm) wavelengths as fluorescein isothiocyanate (FITC). Thus, the FITC channel for general fluorescence microscopy could be used for the imaging analysis.

In situ imaging of HER2 protein detection in breast cancer tissue samples

For further investigation, FFPE specimens with sufficient tissue were retrieved from the Department of Pathology of the First Affiliated Hospital of Chongqing Medical University. This study was approved by the Ethics Committee of the First Affiliated Hospital of Chongqing Medical University (K2023-182). IHC staining FFPE sections were placed on a 60°C baking machine for 2 h and immersed in dimethylbenzene for 8 min. Next, the hydration process was conducted with the following steps using an automatic instrument (Dakewe DP260, China): anhydrous alcohol, 95% ethanol, 85% ethanol, and 75% ethanol; each step for 3 min. Antigen retrieval was achieved by heating in a 10 mM PBS buffer for 20 min at 100°C, cooling to RT, and washing with PBS thrice.

For the breast cancer FFPE sample detection, the HER2 protein was recognized by the oligonucleotide conjugated recombinant anti-HER2 antibody. The conjugated procedure was performed according to the protocol on the commercial kit from Abcam (ab218260). First, the inhibition of the endogenous peroxidase activity and blocking of nonspecific binding sites were consistent with those prior. The oligonucleotide conjugated recombinant anti-HER2 antibody (10 μl 1 mg/ml) was incubated on a slide for 1 h at 37°C. Afterward, the corresponding Co-G4A/H-PER probe was added for another 1 h of hybridization at 37°C. The following fluorescent imaging steps by tyramide deposition were consistent with the cell experiment.

Results

Principle of Co-G4N/H assembly

Building on our previous study, we identified the proximity of vital modules to the catalytic center, such as hemin, the neighboring nucleotide, and G4, as crucial in enhancing catalytic performance. Thus, to develop a more robust and integrated DNAzyme with improved catalytic efficiency, we covalently bound hemin, the adjacent nucleotide, and G4 together to create a self-contained G4 DNAzyme, which has been denoted as Co-G4N/H (N is the acronym for the modified nucleotide). As shown in Fig. 1A, the terminal adenine-modified G4 sequence probe formed a covalent bond with hemin through an amide reaction, forming a Co-G4A/H DNAzyme. The cytosine- and thymine-modified G4 DNAzyme are denoted by Co-G4C/H and Co-G4T/H, respectively. Supplementary Fig. S1 demonstrates the Co-G4A/H structure. The results of mass spectrometry and capillary electrophoresis experiments confirmed the formation of covalent DNA products (Supplementary Figs S2 and S3, and Supplementary Table S2).

Catalytic activity of Co-G4N/H

To investigate the underlying mechanisms, we initially conducted a comparative analysis of the catalytic efficiencies of natural protease HRP, C-G4/H, C-G4A/H, Z-G4A/H, Co-G4/H, and Co-G4A/H (Fig. 1B). In our previous study, three adenine nucleotides yielded better results and achieved saturation [34]; thus, we continued using three nucleotides in this study. The catalytic activity was assessed through the model oxidation reaction of $ABTS^{2-}$, ADHP, and luminol in the pres-

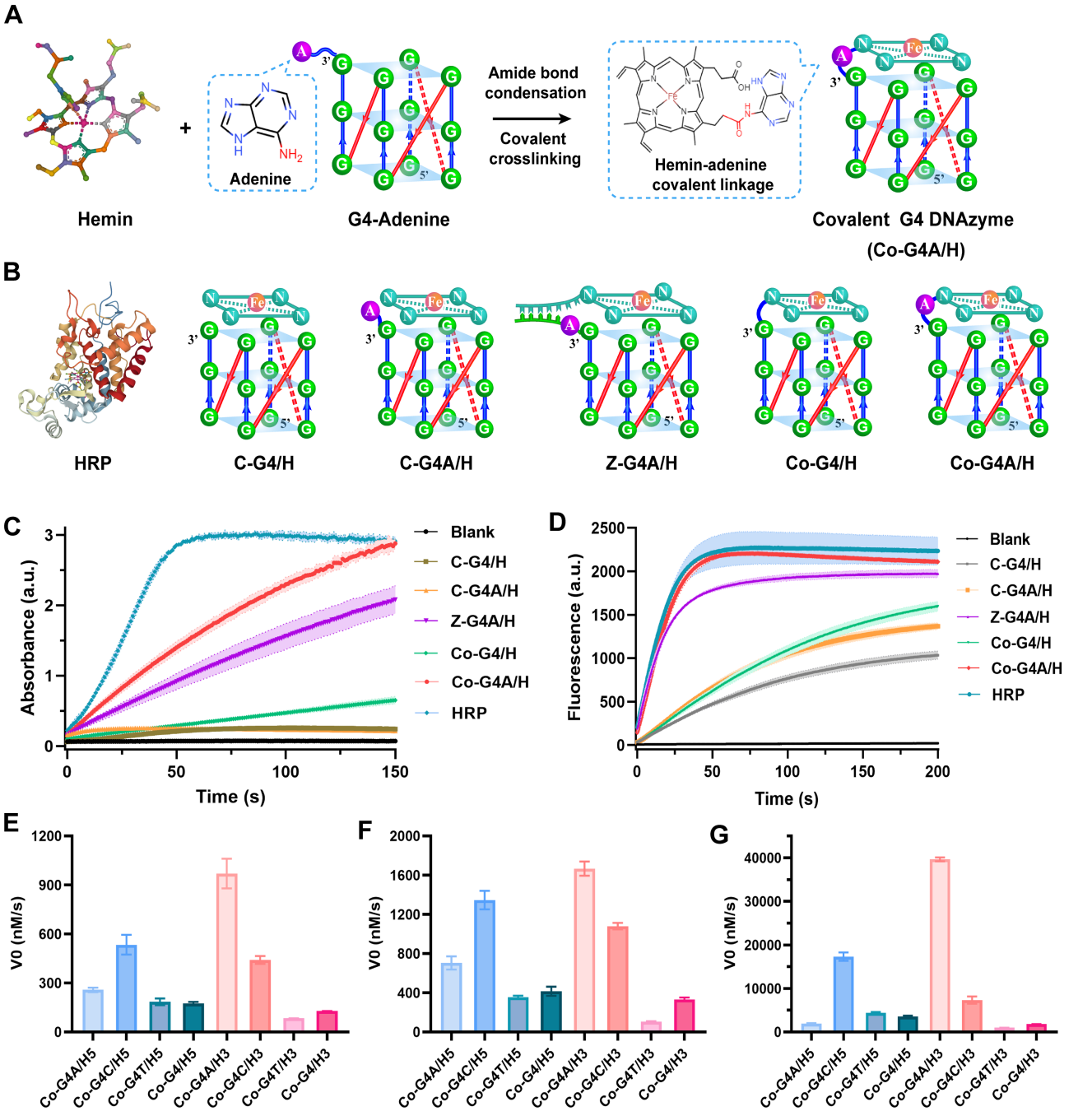

Figure 1 (**A**) Schematic representation of the covalent cross-linking of adenine-modified Co-G4A/H. (**B**) Schematics representations of the assembly structure of HRP and DNAzymes. (**C**) Absorbance kinetic curves of G4 DNAzymes and HRP after incubation with 2 mM $ABTS^{2-}$ and 50 mM H_2O_2. (**D**) Fluorescent kinetic curves of G4 DNAzymes and HRP after incubation with 100 nM ADHP and 1 mM H_2O_2. Activity of G4 DNAzymes (V0, nM/s) after incubation with 2 mM $ABTS^{2-}$ and 50 mM H_2O_2 (**E**), 100 nM ADHP and 1 mM H_2O_2 (**F**), and 2.0 mM luminol and 50 mM H_2O_2 (**G**). The error bars represent the standard deviations of three independent experiments.

ence of H_2O_2 in appropriate concentrations. First, we quantified the amounts of the four aforementioned DNAzymes and HRP using a UV–VIS absorption spectrophotometer. A characteristic peak of hemin was observed at 402 nm [29, 40] (Supplementary Fig. S4), in which the measurements of HRP and DNAzyme were 2 μg/l and 45 nM, respectively. As shown in Fig. 1C, the UV–VIS kinetics of the $ABTS^{2-}$-H_2O_2 system were used to investigate the catalytic efficacy. The initial velocity (V0, nM/s) of Co-G4/H increased compared to the faint peak of C-G4/H, indicating a slight enhancement in the DNAzyme activity due to the efficacy of the covalent linkage by G4 and hemin. Furthermore, a remarkable increase in Co-G4A/H was observed over Co-G4/H, demonstrating that the covalent incorporation of adjacent adenine in the catalytic active center led to superior catalytic performance. Notably, the enhancement effect of noncovalent C-G4A/H is limited. Additionally, Co-G4A/H exhibited a higher catalytic capacity than Z-G4A/H, further narrowing the gap between Co-G4A/H and HRP, confirming that the covalent linkage is a more suitable arrangement. The UV–VIS absorption spectra

of the $ABTS^{2-}$-H_2O_2 system at 418 nm were in line with the pattern observed in the results of the experiments on UV–VIS kinetics (Supplementary Fig. S5A).

The catalytic efficacy was determined by fluorescent kinetics and spectra experiments (Fig. 1D and Supplementary Fig. S5B), and the corresponding initial velocity and absorption peak of the ADHP oxidation results exhibited a trend similar to that in the UV–VIS results. Similarly, the results of the chemiluminescence experiments were consistent with those of the aforementioned kinetics experiments, validating the enhancement of the catalytic activity of Co-G4A/H (Supplementary Fig. S5C) and confirming the robust catalytic efficacy of Co-G4A/H, attributed to the appropriate covalent cross-linking of three components, which substantially narrowed the gap between G4 DNAzyme and HRP.

It is well established that the additional nucleotide (typically adenine or cytosine), functioning as a substitute for the distal histidine of HRP, must be at an optimal distance from the catalytic center to function effectively. For further investigation of the role of adjacent nucleotides in enhancing covalent linkage, we assembled a series of Co-G4N/H variants (Supplementary Fig. S6). As shown in Fig. 1E, Co-G4A/H and Co-G4C/H demonstrated increased catalytic rates. Specifically, Co-G4C/H exhibited a higher initial velocity when hemin and G4 were positioned at the 5′ end of G4 (Co-G4C/H5), whereas Co-G4A/H3 demonstrated an optimal performance when hemin and G4 were located at the 3′ end of G4. Fluorescence kinetics experiments exhibited similar trends to UV–VIS kinetics experiments (Fig. 1F). The absorption and fluorescent spectra are shown in Supplementary Fig. S7. Disparities were observed in the chemiluminescence findings due to the higher catalytic rate of Co-G4C/H5 compared with Co-G4A/H3, which was correlated with substrate selectivity (Fig. 1G).

The relative positioning of key modules is critical, and the optimal arrangement undeniably correlates directly with the optimal catalytic capacity. The catalytic activity of Co-G4N/H decreased when hemin was positioned at the 5′ end of G4 and the nucleotide was positioned at the 3′ end (optimal for enhanced performance), attributable to the separation of hemin and nucleotide, leading to the loss of the optimal arrangement (Supplementary Fig. S8A and B). The catalytic efficiency of Co-G4N/H was reduced when hemin and nucleotide were sequestered together by the T base at the 3′ terminus of G4, due to their separation from the optimal arrangement with the G4 structure (Supplementary Fig. S8C and D). These findings demonstrate the necessity of close association among the three critical modules for the DNAzyme to achieve optimal performance in the covalent mode.

Structural analysis of Co-G4N/H

To elucidate the mechanism underlying the increased catalytic efficiency resulting from the covalent linkage, the structures of a series of Co-G4N/H were determined. First, CD was employed to characterize the Co-G4N/H assembled by various G4 configurations (hybrid, antiparallel, and parallel) (Fig. 2A). As shown in Fig. 2C, the noncovalent antiparallel sequence TA and hybrid G4 PS2.M exhibited weak G4 CD characteristic peaks [17] in the absence of potassium ions, although their CD was significantly enhanced after the covalent linkage. However, these differences are not observed in the presence of potassium ions, which play critical roles in facilitating the formation of G4 configuration (Supplementary Fig. S9). Regardless of the configuration, the catalytic rates increased, following covalent linkage, particularly in a parallel Co-(G3T)A/H DNAzyme (Fig. 2B). These results suggest that the covalent mode enhances hemin solubility [41] and promotes the formation of additional G4 structures, thereby improving the DNAzyme catalytic performance.

The relative orientations of the key modules in the catalytic active center were further investigated via molecular docking experiments on the C-G4A/H3 and Co-G4N/H structures [42, 43]. The findings revealed that irrespective of the covalent modification, the hemin molecules exhibited π–π stacking with the end of the G4 molecules in the five DNAzyme groups. Notably, in all the DNAzyme groups, the Fe atom in the hemin molecule formed coordination interactions with the G base in the terminal G-quadrant, resembling the coordination structure formed between the proximal His170 and hemin in the HRP structure, consistent with the existing literature (Supplementary Fig. S10). Notably, Co-G4A/H3 and Co-G4C/H3 exhibited the shortest coordination distance of 1.7 Å between the hemin active center and G4 when the DNAzyme was covalently modified. However, Co-G4T/H3 (2.1 Å) exhibited a coordination distance that was longer than those of Co-G4/H (1.8 Å) and C-G4A/H3 (2.0 Å) (Fig. 2D). The consistency of the coordination distance with previous catalytic results suggests that the more compact structure of the simulated enzyme may contribute to the high catalytic activity of Co-G4/H. Finally, upon comparing Co-G4A/H3 and Co-G4A/H5, it was observed that the adenine at the 3′ terminal was closer to the coordination center. This may account for the difference in the catalytic capacity between enzymes. These results confirmed that the covalent modification narrowed the distance between the catalytic active centers. A strong association was observed between the catalytic capability and the proximity of the core components. Specifically, a shorter distance corresponds to a more compact structure and enhanced catalytic capability.

Peroxidation behavior and environmental influence of Co-G4N/H

The catalytic activity of the DNAzyme in the $ABTS^{2-}$-H_2O_2 system was primarily demonstrated through its electron transfer rate in the H_2O_2 redox reaction [44]. Thus, to clarify the precise electron mechanism of Co-G4N/H, the impact of adding H_2O_2 on the electronic absorption spectra of the DNAzymes was examined via UV–VIS spectroscopy (Supplementary Fig. S11). Following the addition of H_2O_2, all the DNAzymes exhibited a hypochromicity of the Soret band at 402 nm. The decay rates of the Soret band for Co-G4A/H and Co-G4C/H were substantially higher than that of C-G4A/H, even that of Z-G4A/H (Fig. 3A). The decay rates of Co-G4A/H3 were highest when hemin was labeled at the 3′ end (Fig. 3B), whereas Co-G4C/H5 exhibited the fastest decay at the 5′ end (Fig. 3C). Regardless of the hemin position, Co-G4T/H exhibited the lowest rate. These findings were consistent with the catalytic performance and molecular docking results. They provide evidence that covalently modified DNAzymes can achieve optimal electron transfer rates through the assembly of an optimal configuration, resulting in enhanced catalytic performance. Furthermore, as the initiator and accelerator of the catalytic reaction, insufficient or excessive H_2O_2 leads to poor reaction kinetics [45]. We observed

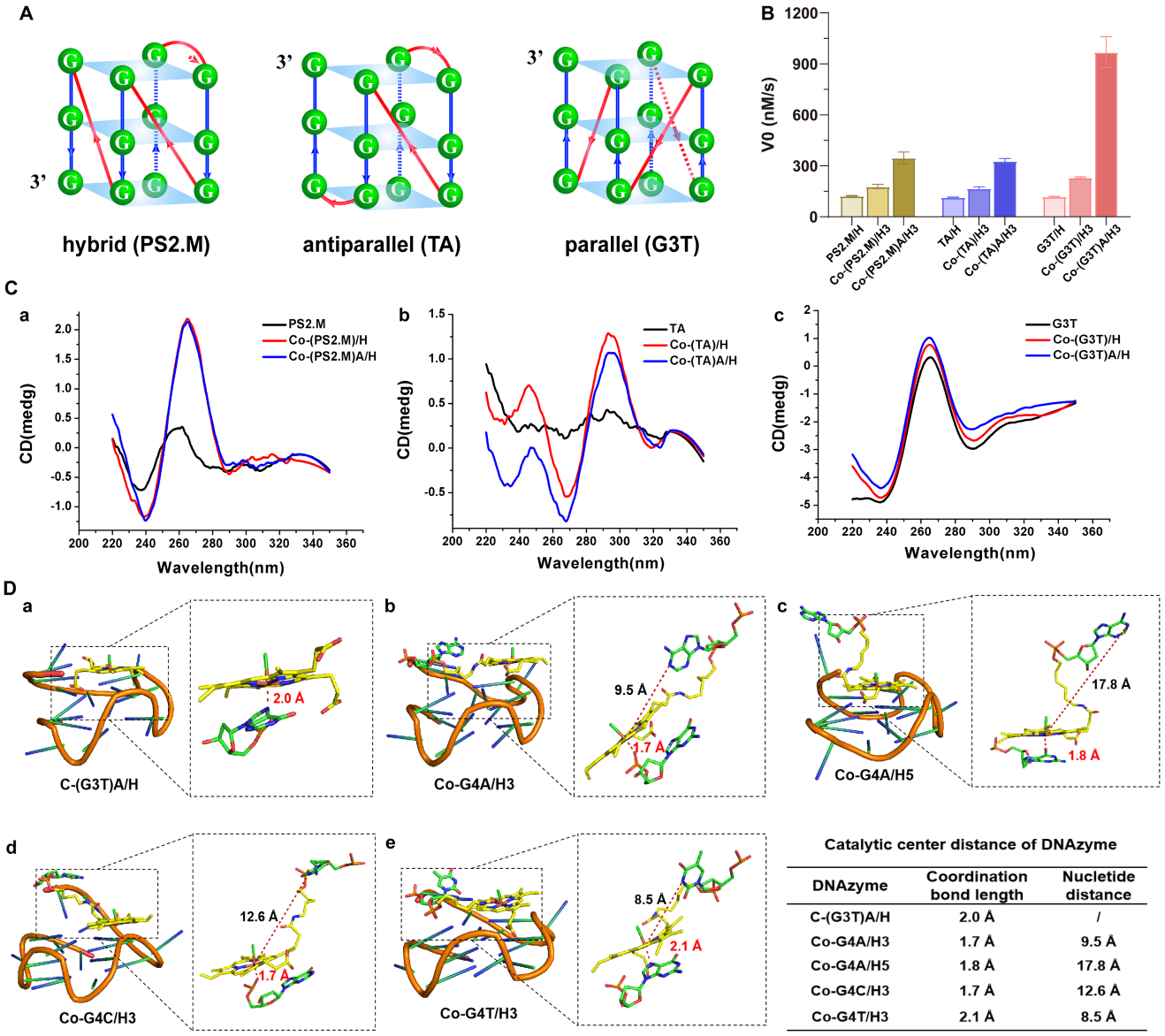

Catalytic center distance of DNAzyme

DNAzyme	Coordination bond length	Nucletide distance
C-(G3T)A/H	2.0 Å	/
Co-G4A/H3	1.7 Å	9.5 Å
Co-G4A/H5	1.8 Å	17.8 Å
Co-G4C/H3	1.7 Å	12.6 Å
Co-G4T/H3	2.1 Å	8.5 Å

Figure 2 (**A**) Schematics of the structures of hybrid (PS2.M), antiparallel (TA), and parallel (G3T) DNAzymes. (**B**) Initial velocity (V0, nM/s) of the hybrid, antiparallel, and parallel DNAzymes after incubation with 2 mM $ABTS^{2-}$ and 50 mM H_2O_2, respectively. (**C**) CD spectra of the hybrid, antiparallel, and parallel DNAzymes. The detection was performed in 50 mM Tris–HCl (pH = 7.0) containing 0 mM KCl and 5 μM DNA at 25°C. (**D**) Molecular simulation results of the interaction mechanism of C-G4/H and Co-G4N/H by molecular docking.

that the initial reaction rate V0 increased with an increase in the H_2O_2 concentration, and the rate of Co-G4A/H notably surpassed that of C-G4A/H and even Z-G4A/H. This finding confirmed the accelerated prototropic cleavage of H_2O_2 in Co-G4A/H, which enhances its exceptional catalytic capacity, owing to the intensive covalent linkage and the nucleotide HRP residue-mimicking structure (Fig. 3E). Additionally, the degradation of hemin is one of the challenges affecting its catalytic applications [46]. To verify the stability of the covalent G4 DNAzyme in this study and whether it degrades, we conducted time-dependent UV–VIS kinetic experiments to profile the catalytic activity of covalent and noncovalent G4 DNAzymes (Supplementary Fig. S12). Reportedly, C-G4A/H began to degrade within 30 s, whereas the Co-G4A/H constructed herein exhibited a signal decline only after 300 s, demonstrating significantly stronger degradation resistance than the former. This observed enhancement may be attributed to the combined effect of the tight spatial protection provided by the Co-G4A/H complex architecture and antioxidant damage resistance conferred by the distal ligand-like adenine nucleotide [46].

A typical pH-dependent rate profile was created to characterize the effect of the adjacent adenine or cytosine on Co-G4N/H as a distal His42 mimic [23]. The results indicated that the dA/dC-modified Co-G4A/H and Co-G4C/H were markedly sensitive to a pH range of 4–6 [14], contrary to the Co-G4/H without nucleotide modifications, which exhibited low activity and near pH insensitivity (Fig. 3D). The marked differences in the pH-rate profiles of the DNAzymes suggested that the dA/dC modification as the endogenous active species mimics the role of amino acid residue in protease functioning as a general acid–base catalyst and substantially enhances the catalytic capability of Co-G4A/H. The pH acceleration phase of Co-G4A/H preceded that of Co-G4C/H, aligning

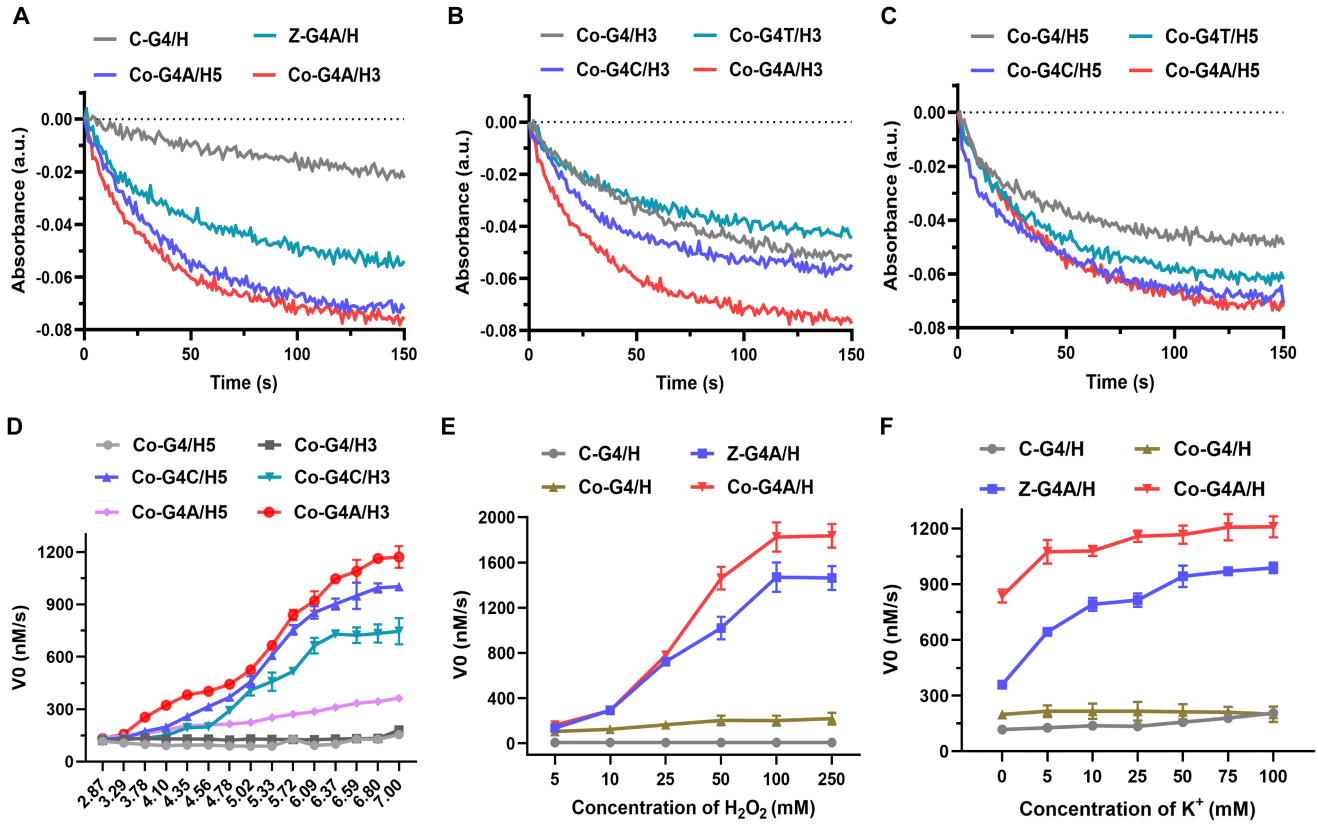

Figure 3 (**A**) Decay kinetics of C-G4/H, Z-G4A/H, Co-G4A/H5, and Co-G4A/H3 at 402 nm in the presence of H_2O_2 (2 mM). Decay kinetics of Co-G4N/H3 (**B**) and 2 μM Co-G4N/H5 (**C**) at 402 nm in the presence of H_2O_2 (2 mM). (**D**) DNAzyme activity of the six DNAzymes as a function of pH. DNAzyme activity of C-G4/H, Z-G4A/H, Co-G4/H, and Co-G4A/H as a function of the H_2O_2 substrate concentration (**E**) and K^+ concentration (**F**), respectively. The error bars represent the standard deviations of three independent experiments.

with the disparity in the pKa values between ATP and CTP (the pKa values of ATP.H+/ATP and CTP.H+/CTP are 3.6 and 4.1, respectively) [25], demonstrating the dominant roles of Co-G4A/H and Co-G4C/H, respectively.

It is noteworthy that previous reports suggest that G4 structures may undergo transformation at pH < 4 [47], which could also contribute to the reduced catalytic activity of G4 DNAzyme at such pH values in this study. All the pH accelerations of Co-G4N/H, as mentioned above, are consistent with their catalytic capacity, substantiating the significant contributions of adenine and cytosine to DNAzyme construction.

K^+ plays a significant role in stabilizing DNAzymes for G4 topology folding [48]. As shown in Fig. 3F, the increase in potassium ion concentration led to significant changes in Co-G4A/H and Co-G4C/H. The plateau phase of Co-G4A/H was achieved with a lower potassium ion concentration (5 mM) compared with that of Co-G4C/H, which requires ~25 mM. Furthermore, Co-G4A/H exhibited the highest V0 in the absence of potassium ions compared with the other three DNAzymes. Additionally, to eliminate the ionic strength effect, we investigated the catalytic activity with lithium ion (Li^+) employed as a control. Li^+ did not have any enhancement effects on the catalysis, confirming that K^+ indeed promotes G4 catalysis (Supplementary Fig. S13). These findings demonstrate that the covalent assembly mode of Co-G4A/H is more efficient than additional zippered hybridization and noncovalent ion-assisted assembly, as it can be assembled without the assistance of ions.

Investigating the catalytic capability of Co-G4N/H in localized droplets

The catalytic capacity of enzymes in confined spaces is essential for biosensing applications that are dependent on enzyme-catalyzed interfaces. It is significant for the highly sensitive detection of low-concentration targets, particularly in the enzyme catalysis of the imaging analysis of diagnostic applications [49, 50]. Thus, following the successful construction of Co-G4A/H with high efficiency and a ready-made assembly, we investigated its catalytic capabilities in localized droplets and anticipated its potential in localized catalytic applications at interfaces. DNAzymes with ADHP substrates and H_2O_2 were separately introduced into the microfluidic chip through distinct channels, resulting in the formation of water-in-oil droplets containing a DNAzyme catalytic system, generating digital out-of-fluorescence signals for the analysis of the DNAzyme catalytic capability in localized droplets in the order of microliters (Fig. 4A).

To assess the catalytic activity of Co-G4N/H in localized droplets, we comparatively analyzed Co-G4A/H3, Co-G4/H3, C-G4/H, and the natural protease HRP. Based on the hemin cofactor quantification, the DNAzyme concentration was 9 nM when HRP was 0.4 μg/ml, and we continued to use this enzyme concentration in the droplet system. After incubating the enzyme-catalyzed droplets at RT for 5 min, they were observed in the microfluidic chip observation cell (Fig. 4B). The fluorescence intensity of Co-G4/H3 significantly exceeded that of noncovalent C-G4/H, with adenine-

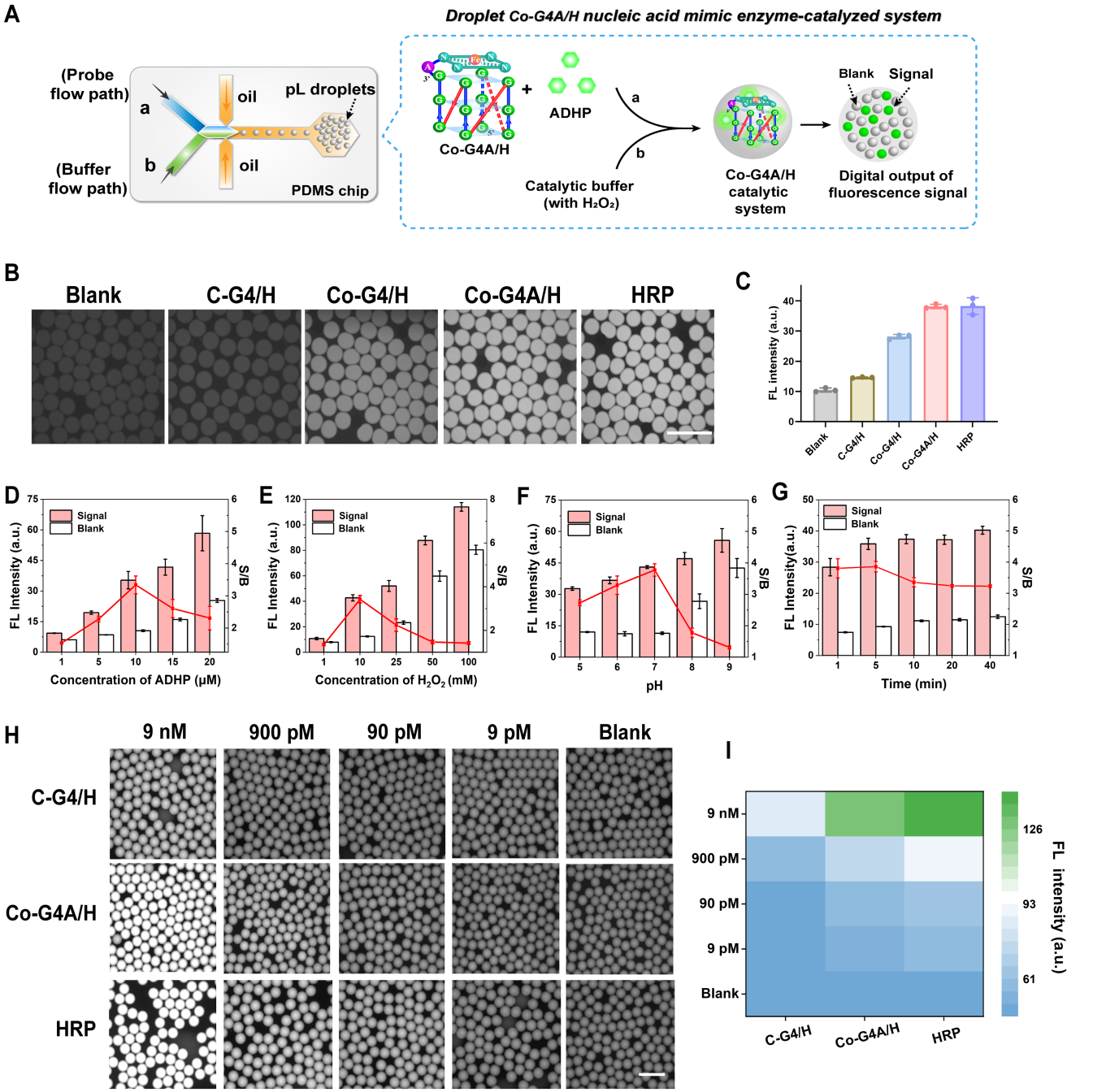

Figure 4 (**A**) Schematics of the Co-G4A/H nucleic mimic enzyme-catalyzed system in localized droplets. Fluorescence imaging analysis (**B**) and fluorescence quantitative analysis (**C**) of C-G4/H, Co-G4/H3, Co-G4A/H, and HRP-catalyzed droplets in the microfluidic chip observing groove by incubating at RT after 5 min. Optimization of Co-G4A/H3 liquid drop catalytic system at (**D**) substrate ADHP concentration, (**E**) H_2O_2 concentration, (**F**) buffer pH, and (**G**) incubation time at RT. Fluorescence imaging analysis (**H**) and fluorescence quantitative analysis (**I**) of enzyme concentration gradients. The enzyme-catalyzed droplets were collected in a test tube and incubated at RT for 6 h. Scale bar: 250 μm. The error bars represent the standard deviation of three independent experiments.

modified Co-G4A/H3 exhibiting a catalytic capacity comparable to HRP. These findings were further supported by the fluorescence quantification results obtained using ImageJ (Fig. 4C), indicating that Co-G4A/H3 exhibited a catalytic capacity similar to that of HRP in droplets.

For further investigation, we optimized four key experimental factors (substrate ADHP concentration, H_2O_2 concentration, reaction time, and buffer pH) to enhance the enzymatic activity. The results indicated that the optimal substrate concentration for Co-G4A/H3 catalysis in the droplet was 10 μM (Fig. 4D), and the H_2O_2 concentration was 10 mM (Fig. 4E). Figure 4F shows that the signal-to-noise ratio reached its maximum when the enzyme-catalyzed droplet was incubated for 5 min at RT for detection, with a gradual decrease with an increase in the incubation time. The buffer pH of the droplet system may impact droplet stability and subsequently affect the Co-G4A/H3 catalysis. As shown in Fig. 4G, the highest signal-to-noise ratio of Co-G4A/H3 catalysis was achieved at

a buffer pH of 7. The corresponding fluorescence imaging of the droplets is shown in Supplementary Fig. S14.

Based on the optimized enzymatic reaction conditions, we investigated the minimum catalytic concentration of Co-G4A/H and HRP in the optimal droplet system. Considering the volatility of HFE-7500 and the slow enzymatic reaction rate at a low enzyme concentration, we collected the generated droplets using a centrifuge tube and transferred them onto a slide to observe them and obtain images. As shown in Fig. 4H, naked-eye observation revealed that the fluorescent droplets catalyzed by Co-G4A/H3, C-G4/H, and HRP were distinguishable from the background. Fluorescence quantification was conducted using the ImageJ for comparison (Fig. 4I). The results showed that Co-G4A/H3 and HRP were distinguishable from the background at a minimal concentration of 9 pM, whereas traditional C-G4/H required 900 pM, demonstrating that the covalent linkage Co-G4A/H3 exhibited a catalytic ability comparable to that of HRP in such localized droplets. The efficient localized catalytic capability of Co-G4A/H3 indicates its potential for highly sensitive imaging applications with low-abundance targets at interfaces.

Practical applications of Co-G4N/H in *in situ* imaging

As a crucial protein marker in breast cancer, the accurate assessment of HER2 protein expression is essential for clinical management and prognostic prediction in patients [36]. Given the enhanced catalytic capability of Co-G4A/H and its DNA programmability, we integrated Co-G4A/H with PER isothermal amplification for HER2 protein *in situ* imaging. The PER is an emerging isothermal amplification technology that can efficiently amplify long single-stranded DNA with a specific sequence under the catalysis of DNA polymerase [51]. Recently, it has been applied in the field of biosensing, demonstrating its potential for advancing molecular detection methods. Here, the HER2 protein was initially identified using the HER2-apt probe comprising a HER2 aptamer and PER sequence. A long single strand with a specific sequence generated by PER amplification was subsequently introduced, followed by incubation with the Co-G4A/H probe. The highly sensitive *in situ* imaging of the HER2 protein was achieved through catalytic fluorescent tyramine deposition on the cell surface. To enhance sensitivity, we explored the efficacy of two-branch PER amplification, specifically PER-B1 and PER-B2. A control system using Fluor-488 fluorescent and C-G4A/H probes combined with PER and HRP-based tyramine signal amplification strategy (TSA) catalysis was developed for the assay.

The PER amplification efficiency was confirmed through PAGE validation, demonstrating the feasibility of PER and the two-branch PER (Supplementary Fig. S15). We assessed the catalytic capability of Co-G4A/H-PER amplification in a 96-well plate. HER2 mRNA functioned as the target, and the Co-G4A/H-PER catalytic system was introduced to validate the signal output ability of the Co-G4A/H-PER probe by catalyzing the ADHP/H_2O_2 substrate. Fluor-488-PER and C-G4A/H-PER probes were used as controls. The results demonstrated evident fluorescence signals from the three groups of signal probes following hybridization, confirming the successful hybridization of the PER amplification product with the signal probe (Supplementary Fig. S16). Regarding catalytic activity, the Co-G4A/H-PER probe exhibited a lower detection limit compared with the control Fluor-488-PER and C-G4A/H-PER groups (0.61 nM versus 1.63 and 2 nM), suggesting its promising application potential for the imaging detection of the HER2 protein.

The aforementioned results have demonstrated the feasibility of a Co-G4A/H-PER-based HER2 protein *in situ* detection strategy, which was further validated on the cell surface. SKBR3 cells with positive HER2 expression were used as a model, and the fluorescence images of the cells were captured using an inverted fluorescence microscope. Aptamer sequences targeting the HER2 protein were initially screened. As shown in Supplementary Fig. S17A, the aptamer 2 sequence yielded a complete and robust fluorescence signal and was consequently selected as the final aptamer sequence in this study. We optimized the tyramine fluorescent substrate and H_2O_2 concentration in the catalytic system, determining that the optimal ratio and concentration of the tyramine substrate (Tyr-488) and H_2O_2 were 1:200 and 0.03%, respectively (Supplementary Fig. S17B and C).

Under optimal experimental conditions, we developed a highly sensitive imaging detection strategy based on Co-G4A/H-PER to visualize SKBR3 cells (Fig. 5A). The proficiency test of PER and its two-branch PER on SKBR3 cell surface imaging detection was conducted. Fluor-488-PER and C-G4A/H-PER systems were employed as controls. As shown in the fluorescence imaging figure and the quantified fluorescence values obtained using ImageJ (Fig. 5B and C), the fluorescence signals of the three systems were enhanced with an increase in the PER branches, with Co-G4A/H-PER exhibiting the highest signal intensity at each level. The secondary branch signal enhancement of Fluor-488-PER was minimal, possibly due to potential quenching effects from fluorescent probe stacking commonly observed in DNA assembly. Compared with commercial HRP-based TSA kits, Co-G4A/H-PER consistently demonstrated superior signal amplification attributed to efficient Co-G4A/H combination and isothermal amplification technology, confirming the efficacy of the proposed strategy.

Finally, to validate the feasibility of this approach, SKBR3 cells were used as a positive cell model while HER2-negative MDA-MB-231 and MCF-7 cells with low HER2 expression functioned as controls. No discernible fluorescence signal was detected in MDA-MB-231 or MCF-7 cells; however, a solid green fluorescence signal was observed on the surface of SKBR3 cells with high HER2 expression (Fig. 5D). Flow cytometry experiments confirmed these observations (Fig. 5E), demonstrating the viability and specificity of the Co-G4A/H-PER-based *in situ* protein detection strategy for cell surface HER2 protein detection.

We validated the proposed strategy using 16 clinical FFPE breast cancer samples to assess its clinical applicability. All the samples underwent initial semi-quantitative analysis for HER2 protein via clinical IHC and were categorized into HER2 3+, HER2 2+, HER2 1+, and HER2 negative (HER2 0) four subgroups (four cases of each) based on the American Society of Clinical Oncology scoring system and IHC staining results. The HER2 protein expression of the specimens was assessed using the highly efficient Co-G4A/H-PER *in situ* detection strategy (Fig. 6A). First, sodium dodecyl sulfate–polyacrylamide gel electrophoresis experiments confirmed the successful conjugation of the antibodies and oligonucleotide sequences (Supplementary Fig. S18). In Fig. 6B and Supplementary Fig. S19, the green fluorescence in the

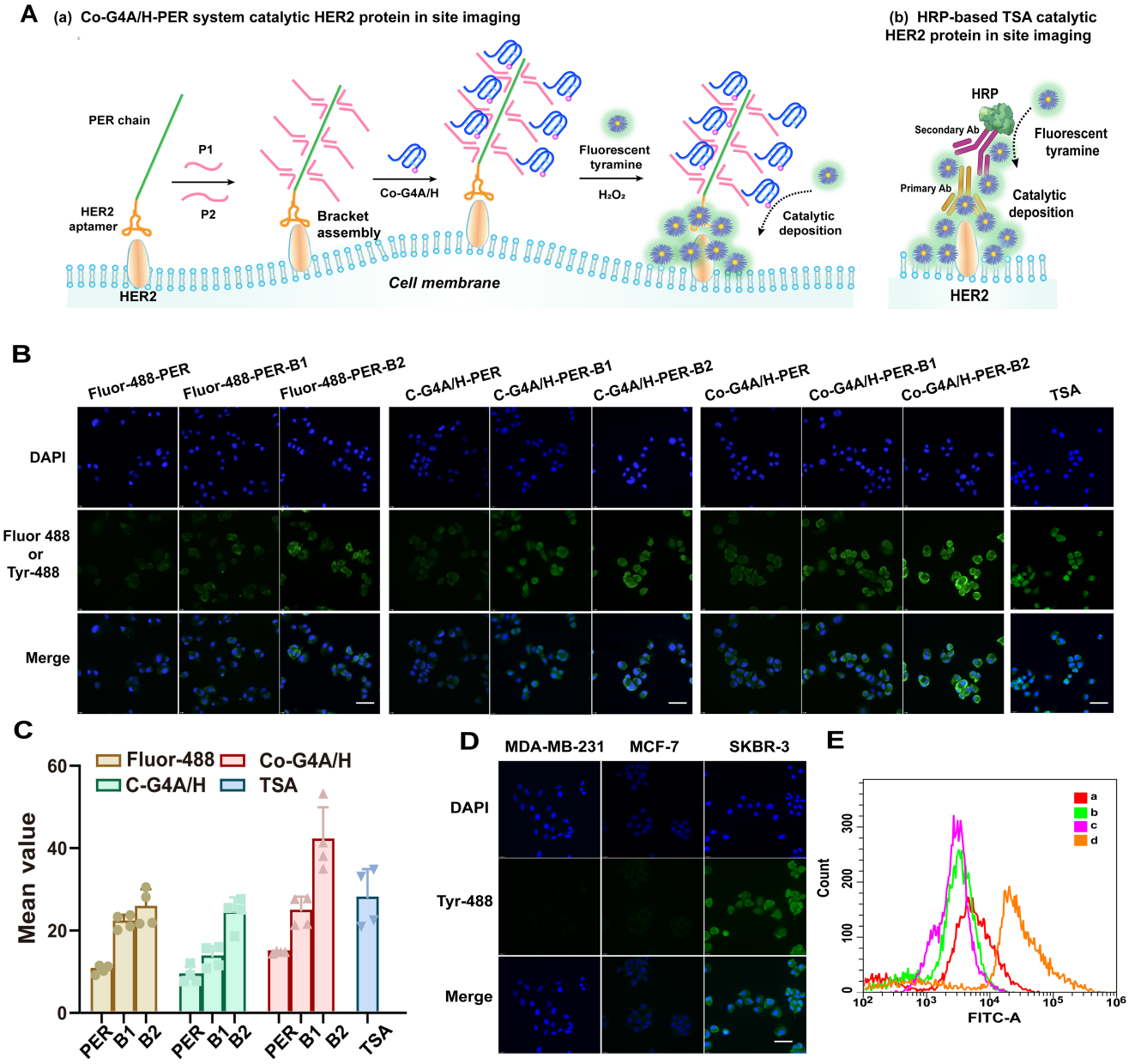

Figure 5 (**A**) Schematic of Co-G4A/H-PER system (a) and HRP-based TSA (b) catalyzing the substrate tyramine-fluorophore for the sensitive detection of HER2 protein on breast cancer cells. (**B**) Fluorescence imaging and (**C**) quantification of SKBR-3 breast cancer cells using the Fluor-488-PER, C-G4A/H-PER, and Co-G4A/H-PER systems by ImageJ. (**D**) Fluorescence imaging of SKBR-3, MCF-7, and MDA-MB-231 cells using the Co-G4A/H-PER system. Scale bar: 25 μm. (**E**) Flow cytometric analysis of (a) blank control, (b) MDA-MB-231, (c) MCF-7, and (d) SKBR-3 cells using the Co-G4A/H-PER system.

tissue samples gradually increased with increased levels of HER2 expression, consistent with the IHC findings. Prominent green fluorescence was observed in tissues with high expression of HER2 (HER2 3+ and HER2 2+), whereas only weak green fluorescence was detected in tissues with low expression of HER2 (HER2 1+ and HER2 negative). Using the proposed approach, we achieved an accurate grading of HER2 protein expression through fluorescence (Fig. 6C), consistent with the IHC results (all quantified using ImageJ) (Fig. 6D). These findings show that the Co-G4A/H-PER-based strategy for detecting HER2 protein exhibits strong specificity and feasibility when applied to clinical samples, thereby facilitating precise molecular tumor typing and targeted therapy.

Discussion

Based on our previous research and the existing literature, the positioning and proximity of the key core modules in the catalytic active center of G4 DNAzymes are crucial in enhancing catalytic efficiency. These core modules include the hemin cofactor, backbone G4 sequence, and nucleotide ligand. Neither the traditional weak π–π stacking of C-G4/H nor the zippered hybridization of Z-G4/H can lead to intermolecular assemblies between the core modules. Consequently, they cannot establish a more tightly integrated catalytic active center for enhanced catalytic capacity or acting as readily available catalytic modules for practical applications. Thus, to enhance the catalytic capability and address the limitations as-

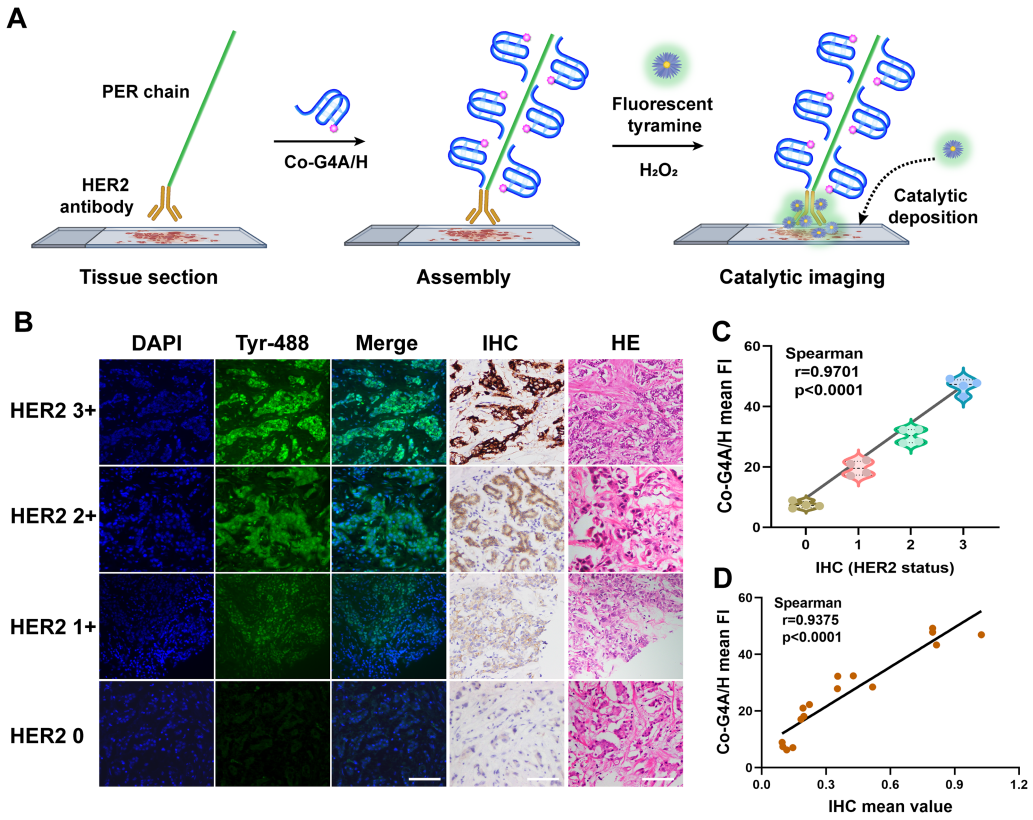

Figure 6 (**A**) Schematic of the Co-G4A/H-PER system catalyzing the substrate tyramine-488 for the sensitive detection of HER2 protein on the FFPE sample of patients with breast cancer. (**B**) Fluorescence, IHC, and HE imaging of HER2 protein quantitative grading on an FFPE sample of patients of breast cancer using a Co-G4A/H-PER system. (**C**) Spearman's rank correlation coefficient analysis between HER2 protein quantitative grading and the fluorescence quantification value by ImageJ from fluorescence imaging. (**D**) Spearman's rank correlation coefficient analysis between Co-G4A/H-PER and the IHC mean value. Scale bar: 25 μm.

sociated with assembly requirements, this study focused on the covalent linkage of the hemin, ligand nucleotide, and G4 structure through amide reaction to develop a compact and efficient intramolecular covalent G4 DNAzyme (Co-G4N/H). Through designing a series of Co-G4N/H with different modification positions of hemin, diverse types and positions of nucleotide modifications, and various G4 topologies, we investigated the catalytic performance and established general rules for the efficient assembly of Co-G4N/H. The study findings demonstrate that the (i) covalent attachment of hemin ligands to adenine- or cytosine-modified G4 ends can enhance the proximity of the G4 DNAzyme core modules, promoting the formation of more G4 DNAzyme structures and facilitating higher electron transfer rates during catalytic reactions, thereby enhancing the activity of G4 DNAzymes. (ii) Adenine or cytosine modifications near the active site may mimic the effect of His42 in enhancing the catalytic activity of HRP and augment the catalytic capability of Co-G4N/H. The location and distance of nucleotide ligands in the active center of G4 DNAzymes affect its catalytic ability, with shorter distances to the active center are correlated with more robust catalytic capabilities. (iii) Compared with C-G4/H, Co-G4N/H exhibits reduced dependence on metal ions and does not require an further assembly steps; thus, it is advantageous in complex environments in the pre-assembled form.

The Co-G4A/H3 catalyst with superior performance was employed in the localized environments to investigate its catalytic activity and potential for confined-space catalysis, demonstrating an efficacy comparable to that of HRP in the droplet-based system. Moreover, G4 DNAzyme exhibits higher thermal stability and a broader pH tolerance range compared with HRP [13]. Additionally, its DNA programmability endows it with extensive application potential in molecular diagnostics and various tasks, including isothermal amplification and IHC. Therefore, we harnessed the high catalytic efficiency and DNA programmability of Co-G4A/H3, integrating it with PER isothermal amplification technology to enable the *in situ* imaging of HER2 protein in cells and tissues. Notably, the proposed approach enabled the accurate grading of HER2 protein expression in clinical tissue samples, exhibiting a high degree of concordance with conventional clinical IHC technology. The highly efficient and ready-made catalytic signal reporting element Co-G4N/H showed excellent potential for clinical application in imaging analysis. This study provides a fresh perspective for investigating the catalytic capacity of G4/hemin DNAzymes, offering a practical detection tool for identifying low-abundance markers in clinical settings.

Acknowledgements

We are grateful for helpful discussions on the pathological diagnosis of breast cancer with PhD Li Wang and Yixin Li at the Chongqing Medical University in China.

Author contributions: J.L.: Conceptualization, Investigation, Methodology, Formal analysis, Writing—original draft,

Writing—review & editing. L.X.J.: Investigation, Methodology, Data curation, Writing—original draft. H.P.W.: Investigation, Project administration, Software, Writing—review & editing. Y.T.Z.: Software, Validation. S.S.Z., Y.H., and X.P.H.: Resources, Visualization, Validation. H.L.B., Y.L., and Y.Z.: Resources, Software. S.J.D.: Supervision, Validation, Resources. W.C.: Conceptualization, Resources, Project administration, Supervision, Writing—review & editing, Funding acquisition. All authors have read and agreed to the published version of the manuscript.

Supplementary data

Supplementary data is available at NAR online.

Conflict of interest

None declared.

Funding

This work was funded by the National Natural Science Foundation of China (U24A20751, 82202634, 82402750, and 82372334), the special funding project of Chongqing Municipality (2023CQBSHTB3058), Chongqing Medical Young Talents Project (YXQN202435), Science and Technology Research Project of Chongqing Education Commission (KJQN202400411), China Postdoctoral Science Foundation (2024MD764067), Sichuan Science and Technology Program (2024NSFSC1541), Young Top Talent Project of the First Affiliated Hospital of Chongqing Medical University (BJRC2022-02), Chongqing Medical Scientific Research Project (joint project of Chongqing Health Commission and Science and Technology Bureau) (2022QNXM007), CQMU Program for Youth Innovation in Future Medicine (W0149).

Data availability

The data supporting the findings of this study are available within the paper and its Supplementary Information, and additional data are available from the corresponding author on reasonable request.

References

1. Huang Y, Ren J, Qu X. Nanozymes: classification, catalytic mechanisms, activity regulation, and applications. *Nature* 2019;**119**:84–9. https://doi.org/10.1021/acs.chemrev.8b00672
2. Zhou Z, Roelfes G. Synergistic catalysis in an artificial enzyme by simultaneous action of two abiological catalytic sites. *Nature Catalysis* 2020;**3**:289–94. https://doi.org/10.1038/s41929-019-0420-6
3. Hu X, Zhang B, Zhang M *et al.* An artificial metabzyme for tumour-cell-specific metabolic therapy. *Nat Nanotechnol* 2024;**19**:1712–22. https://doi.org/10.1038/s41565-024-01733-y
4. Bhuyan SK, Wang L, Jinata C *et al.* Directed evolution of a G-quadruplex peroxidase DNAzyme and application in proteomic DNAzyme-aptamer proximity labeling. *J Am Chem Soc* 2023;**145**:12726–36. https://doi.org/10.1021/jacs.3c02625
5. He L, Chen F, Zhang D *et al.* Transducing complex biomolecular interactions by temperature-output artificial DNA signaling networks. *J Am Chem Soc* 2020;**142**:14234–9. https://doi.org/10.1021/jacs.0c05453
6. Stefan L, Denat F, Monchaud D. Deciphering the DNAzyme activity of multimeric quadruplexes: insights into their actual role in the telomerase activity evaluation assay. *J Am Chem Soc* 2011;**133**:20405–15. https://doi.org/10.1021/ja208145d
7. Nakayama S, Wang J, Sintim HO. DNA-based peroxidation catalyst–what is the exact role of topology on catalysis and is there a special binding site for catalysis? *Chem* 2011;**17**:5691–8. https://doi.org/10.1002/chem.201002349
8. Poon LC, Methot SP, Morabi-Pazooki W *et al.* Guanine-rich RNAs and DNAs that bind heme robustly catalyze oxygen transfer reactions. *J Am Chem Soc* 2011;**133**:1877–84. https://doi.org/10.1021/ja108571a
9. Sen D, Poon LC. RNA and DNA complexes with hemin [Fe(III) heme] are efficient peroxidases and peroxygenases: how do they do it and what does it mean? *Crit Rev Biochem Mol Biol* 2011;**46**:478–92. https://doi.org/10.3109/10409238.2011.618220
10. Einarson OJ, Sen D. Self-biotinylation of DNA G-quadruplexes via intrinsic peroxidase activity. *Nucleic Acids Res* 2017;**45**:9813–22. https://doi.org/10.1093/nar/gkx765
11. Dehui Q, Fangni H, Yuan L *et al.* A cost-effective hemin-based artificial enzyme allows for practical applications. *Adv Sci (Weinh)* 2024;**11**:e2402237.
12. Chen Y, Qiu D, Zhang X *et al.* Highly sensitive biosensing applications of a magnetically immobilizable covalent G-quadruplex-hemin DNAzyme catalytic system. *Anal Chem* 2022;**94**:2212–9. https://doi.org/10.1021/acs.analchem.1c04842
13. Guo Y, Chen J, Cheng M *et al.* A Thermophilic tetramolecular G-quadruplex/hemin DNAzyme. *Angew Chem Int Ed Engl* 2017;**56**:16636–40. https://doi.org/10.1002/anie.201708964
14. Wang L, Yong L, Zhuoliang L *et al.* Insight into G-quadruplex-hemin DNAzyme/RNAzyme: adjacent adenine as the intramolecular species for remarkable enhancement of enzymatic activity. *Nucleic Acids Res* 2016;**44**:7373–84. https://doi.org/10.1093/nar/gkw634
15. Lv S, Zhang K, Lin Z *et al.* Novel photoelectrochemical immunosensor for disease-related protein assisted by hemin/G-quadruplex-based DNAzyme on gold nanoparticles to enhance cathodic photocurrent on p-CuBi2O4 semiconductor. *Biosens Bioelectron* 2017;**96**:317–23.https://doi.org/10.1016/j.bios.2017.05.027
16. Zhang K, Lv S, Lin Z *et al.* CdS:mn quantum dot-functionalized g-C3N4 nanohybrids as signal-generation tags for photoelectrochemical immunoassay of prostate specific antigen coupling DNAzyme concatamer with enzymatic biocatalytic precipitation. *Biosens Bioelectron* 2017;**95**:34–40. https://doi.org/10.1016/j.bios.2017.04.005
17. Farag M, Mouawad L. Comprehensive analysis of intramolecular G-quadruplex structures: furthering the understanding of their formalism. *Nucleic Acids Res* 2024;**52**:3522–46. https://doi.org/10.1093/nar/gkae182
18. Lv M, Guo Y, Ren J *et al.* Exploration of intramolecular split G-quadruplex and its analytical applications. *Nucleic Acids Res* 2019;**47**:9502–10. https://doi.org/10.1093/nar/gkz749
19. Luo Y, Zivkovic ML, Wang J *et al.* A sodium/potassium switch for G4-prone G/C-rich sequences. *Nucleic Acids Res* 2024;**52**:448–61. https://doi.org/10.1093/nar/gkad1073
20. Ambrus A, Chen D, Dai J *et al.* Human telomeric sequence forms a hybrid-type intramolecular G-quadruplex structure with mixed parallel/antiparallel strands in potassium solution. *Nucleic Acids Res* 2006;**34**:2723–35. https://doi.org/10.1093/nar/gkl348
21. Qi C, Zhang N, Yan J *et al.* Activity enhancement of G-quadruplex/hemin DNAzyme by spermine. *RSC Adv* 2014;**4**:1441–8. https://doi.org/10.1039/C3RA45429K
22. Chang T, Gong H, Ding P *et al.* Activity enhancement of G-quadruplex/hemin DNAzyme by flanking d(CCC). *Chemistry* 2016;**22**:4015–21. https://doi.org/10.1002/chem.201504797
23. Stefan L, Denat F, Monchaud D. Insights into how nucleotide supplements enhance the peroxidase-mimicking DNAzyme activity of the G-quadruplex/hemin system. *Nucleic Acids Res* 2012;**40**:8759–72. https://doi.org/10.1093/nar/gks581
24. Chen J, Guo Y, Zhou J *et al.* The effect of adenine repeats on G-quadruplex/hemin peroxidase mimicking DNAzyme activity.

Chemistry 2017;**23**:4210–5. https://doi.org/10.1002/chem.201700040
25. Chen J, Zhang Y, Cheng M *et al.* How proximal nucleobases regulate the catalytic activity of G-quadruplex/hemin DNAzymes. *ACS Catalysis* 2018;**8**:11352–61. https://doi.org/10.1021/acscatal.8b03811
26. Kosman J. Enhancement of activity for peroxidase-mimicking DNAzyme by covalent attachment of hemin to G-quadruplex-forming oligonucleotide using click chemistry. *Methods Mol Biol* 2022;**2439**:291–9.
27. Gribas AV, Zatsepin TS, Korolev SP *et al.* Suicide inactivation of covalent peroxidase-mimicking DNAzyme with hydrogen peroxide and its protection by a reductant substrate. *Talanta* 2016;**155**:212–5. https://doi.org/10.1016/j.talanta.2016.04.033
28. Thirstrup D, Baird GS. Histochemical application of a peroxidase DNAzyme with a covalently attached hemin cofactor. *Anal Chem* 2010;**82**:2498–504. https://doi.org/10.1021/ac902887j
29. Zhang X, Qiu D, Chen J *et al.* Chimeric biocatalyst combining peptidic and nucleic acid components overcomes the performance and limitations of the native horseradish peroxidase. *J Am Chem Soc* 2023;**145**:4517–26. https://doi.org/10.1021/jacs.2c11318
30. Qiu D, Mo J, Liu Y *et al.* Effect of distance from catalytic synergy group to iron porphyrin center on activity of G-quadruplex/hemin DNAzyme. *Molecules* 2020;**25**:3425. https://doi.org/10.3390/molecules25153425
31. Zozulia O, Korendovych IV. Semi-rationally designed short peptides self-assemble and bind hemin to promote cyclopropanation. *Angew Chem Int Ed Engl* 2020;**59**:8108–12. https://doi.org/10.1002/anie.201916712
32. Li J, Yuan T, Yang T *et al.* DNA-grafted hemin with preferable catalytic properties than G-quadruplex/hemin for fluorescent miRNA biosensing. *Sens Actuators, B* 2018;**271**:239–46. https://doi.org/10.1016/j.snb.2018.05.045
33. Li J, Xiang Y, Zhang L *et al.* Dynamic DNA self-assembly activated hemin-mimetic enzyme system for versatile fluorescent biosensing. *Sens Actuators B Chem* 2019;**288**:757–62. https://doi.org/10.1016/j.snb.2019.03.058
34. Li J, Wu H, Yan Y *et al.* Zippered G-quadruplex/hemin DNAzyme: exceptional catalyst for universal bioanalytical applications. *Nucleic Acids Res* 2021;**49**:13031–44. https://doi.org/10.1093/nar/gkab1178
35. Shumayrikh N, Huang YC, Sen D. Heme activation by DNA: isoguanine pentaplexes, but not quadruplexes, bind heme and enhance its oxidative activity. *Nucleic Acids Res* 2015;**43**:4191–201. https://doi.org/10.1093/nar/gkv266
36. Bueno-Muino C, Echavarria I, Lopez-Tarruella S *et al.* Assessment of a genomic assay in patients with ERBB2-positive breast cancer following neoadjuvant trastuzumab-based chemotherapy with or without pertuzumab. *JAMA Oncol* 2023;**9**:841–6. https://doi.org/10.1001/jamaoncol.2023.0187
37. Zouein J, Karam E, Strickler JH *et al.* Trastuzumab-Deruxtecan: Redefining HER2 as a Tumor Agnostic Biomarker. . *Targeted oncology* 2024;**19**:705–10. https://doi.org/10.1007/s11523-024-01079-4
38. Kishi JY, Lapan SW, Beliveau BJ *et al.* SABER amplifies FISH: enhanced multiplexed imaging of RNA and DNA in cells and tissues. *Nat Methods* 2019;**16**:533–44. https://doi.org/10.1038/s41592-019-0404-0
39. Wu D, Tang J, Yu Z *et al.* Pt/Zn-TCPP nanozyme-based flexible immunoassay for dual-mode pressure–temperature monitoring of low-abundance proteins. *Anal Chem* 2024;**96**:8740–6. https://doi.org/10.1021/acs.analchem.4c01059
40. Wang Q, Xu N, Gui Z *et al.* Catalytic activity of a dual-hemin labelled oligonucleotide: conformational dependence and fluorescent DNA sensing. *Chemistry Commun (Camb)* 2014;**50**:15362–5. https://doi.org/10.1039/C4CC07298G
41. Wang Q, Xu N, Gui Z *et al.* Strand displacement activated peroxidase activity of hemin for fluorescent DNA sensing. *Analyst* 2015;**140**:6532–7. https://doi.org/10.1039/C5AN01206F
42. Dickerhoff J, Warnecke KR, Wang K *et al.* Evaluating molecular docking software for small molecule binding to G-quadruplex DNA. *Int J Mol Sci* 2021;**22**:10801. https://doi.org/10.3390/ijms221910801
43. Gao J, Liang C, Yin J *et al.* Discovery of palbociclib as a potent c-Myc G4 stabilizer for lung cancer treatment using molecular docking, molecular dynamics simulation, and *in vitro* activity evaluation. *Mol Divers* 2024;**28**:3965–77. https://doi.org/10.1007/s11030-023-10789-2
44. Travascio P, Sen D, Bennet AJ. DNA and RNA enzymes with peroxidase activity An investigation into the mechanism of action. *Can J Chem* 2006;**84**:613–9.
45. Travascio P, Witting PK, Mauk AG *et al.* The peroxidase activity of a hemin–DNA oligonucleotide complex: free radical damage to specific guanine bases of the DNA. *J Am Chem Soc* 2001;**123**:1337–48. https://doi.org/10.1021/ja0023534
46. Monte Carlo AR, Fu J. Inactivation kinetics of G-quadruplex/hemin complex and optimization for more reliable catalysis. *ChemPlusChem* 2022;**87**:e202200090. https://doi.org/10.1002/cplu.202200090
47. Yan Y-Y, Tan J-H, Lu Y-J *et al.* G-Quadruplex conformational change driven by pH variation with potential application as a nanoswitch. *Biochim Biophys Gen Sub* 2013;**1830**:4935–42. https://doi.org/10.1016/j.bbagen.2013.06.019
48. Deiana M, Chand K, Jamroskovic J *et al.* A light-up logic platform for selective recognition of parallel G-quadruplex structures via disaggregation-induced emission. *Angew Chem Int Ed Engl* 2020;**59**:896–902. https://doi.org/10.1002/anie.201912027
49. Li T, Wang Y, Liu W *et al.* Nanoconfinement-guided construction of nanozymes for determining H_2O_2 produced by sonication. *Angew Chem Int Ed Engl* 2023;**62**:e202212438. https://doi.org/10.1002/anie.202212438
50. Zhou H, Zhou Y, Bae HY *et al.* Organocatalytic stereoselective cyanosilylation of small ketones. *Nature* 2022;**605**:84–9. https://doi.org/10.1038/s41586-022-04531-5
51. Kishi JY, Schaus TE, Gopalkrishnan N *et al.* Programmable autonomous synthesis of single-stranded DNA. *Nat Chem* 2018;**10**:155–64.

Received: December 13, 2024. **Revised:** March 5, 2025. **Editorial Decision:** March 6, 2025. **Accepted:** March 11, 2025